ACES Asian Chemical Editorial Society

doi.org/10.1002/cnma.202500070

CHEMNANOMAT
Research Article

www.chemnanomat.org

Optimized Electrochemical Behavior of Carbon-Coated Ti-Doped $Na_3V_2(PO_4)_2F_3$ Cathodes for Sodium-Ion Batteries

Pathak Rajkumar Babunar, Sameer Tirkey, and Ananta Sarkar*

$Na_3V_2(PO_4)_2F_3$ (NVPF) has emerged as a very promising cathode material for sodium-ion batteries (SIBs), on account of its durable structural reliability and impressive electrochemical performance. However, their practical use is limited by low capacity, poor conductivity, slow Na-ion transport, and capacity fading, requiring structural and surface modifications. To overcome its inherent low conductivity, carbon-coated Ti-doped NVPF (designated as NVPF-Ti-x) is prepared via a sol–gel process, with x values of 0, 0.01, 0.02, 0.03, 0.04, and 0.05. Among these variants, NVPF-Ti-0.02 demonstrates the most remarkable electrochemical behavior of high reversible capacity and rate capability. NVPF-Ti-0.02 achieves an exceptional stabilized specific capacity of 133 mAh g^{-1} at a current density of 50 mA g^{-1} after the first cycle onward. It shows a high reversible capacity retention of 94.76% after 100 cycles and 81% after 300 cycles. These results highlight the effectiveness of Ti doping and carbon coating in significantly boosting the conductivity and mechanical stability of NVPF. The improved performance of NVPF-Ti-0.02 underscores its potential as a leading candidate for advanced SIB technologies, offering both high capacity and robust cycling stability.

1. Introduction

Sodium-ion batteries (SIBs) have gained significant attention as a viable solution for wide-scale energy-storage systems due to the abundant availability of sodium, lower cost compared to lithium, enhanced safety, and reliable performance even at low temperatures.[1] The key advantage is the compatibility with aluminum current collectors, as sodium does not form alloys with aluminum, making it a more economical alternative to the copper typically used in lithium-ion batteries (LIBs).[2] Despite these benefits, SIBs face challenges due to the significant ionic radius and mass of sodium ions, leading to slow kinetics and notable structural degradation over repeated intercalation/extraction cycles.[3,4] Although considerable breakthroughs have been made in researching cathode, anode materials, and electrolytes for SIBs, the number of suitable cathode materials remains limited due to the larger ionic size of Na^+ compared to Li^+, which hinders efficient and reversible sodium-ion insertion and extraction in many host materials.[5,6] Consequently, only a few cathode materials can effectively accommodate sodium ions while maintaining good electrochemical performance, highlighting the need for continued innovation in SIB development.

The cathode materials utilized in SIBs encompass a diverse range of compounds, each with distinct characteristics. These include transition metal oxides such as $NaMnO_2$, $NaFeO_2$, $NaCoO_2$, NaV_2O_5, and $NH_4V_4O_{10}$;[7–11] polyanionic compounds including $NaFePO_4$, $Na_3V_2(PO_4)_3$, and $Na_3V_2(PO_4)_2F_3$;[12–14] and Prussian blue analogues (PBAs) like $Na_2MnFe(CN)_6$, $Na_2FeFe(CN)_6$, and $Na_2CoFe(CN)_6$.[15–17] Transition metal oxides are often prone to moisture absorption and air reactivity, which adversely affects their electrochemical performance. This susceptibility limits their practicality for long-term use under ambient conditions.[18,19] These materials may suffer irreversible capacity loss due to transition metal migration into sodium layers, affecting cycling stability. In contrast, PBAs offer strong structural stability and high rate capability via their open 3D channels, though challenges remain in removing crystalline water and preventing metal ion degradation.[20,21] Polyanionic cathode materials, such as $Na_3V_2(PO_4)_2F_3$ (NVPF), present a robust and stable 3D network that allows for effective sodium ion insertion and extraction helps superior rate and better cycling performance in contrast to various cathode materials, making them a promising choice for improving the efficiency and longevity of SIBs.[22,23]

$Na_3V_2(PO_4)_2F_3$, an ideal example of the sodium superionic conductor (NASICON) family, is distinguished as a highly viable cathode material for SIBs on account of its exceptional properties.[24] Among its notable features are a high discharge potential, averaging 3.95 V with respect to Na/Na^+, along with a theoretical capacity of 128 mAh g^{-1}, both of which significantly enhance its energy-storage capabilities. Additionally, NVPF exhibits impressive structural stability and remarkable ionic conductivity, contributing to its strong performance and durability in battery applications.[25] The NVPF compound features an open 3D structure composed of $[V_2O_8F_3]$ dioctahedral units linked with $[PO_4]$ tetrahedral units through repetitive connections via oxygen atoms.[26,27] This unique 3D arrangement creates extensive interstitial spaces, facilitating the rapid and efficient diffusion of Na^+ ions through interconnected channels. This design minimizes volume fluctuations throughout charge and discharge cycles, which

P. R. Babunar, S. Tirkey, A. Sarkar
Department of Chemical Engineering
Indian Institute of Technology Kharagpur
Kharagpur, West Bengal 721302, India
E-mail: ananta@che.iitkgp.ac.in

P. R. Babunar
School of Energy Science and Engineering
Indian Institute of Technology Kharagpur
Kharagpur, West Bengal 721302, India

Supporting information for this article is available on the WWW under https://doi.org/10.1002/cnma.202500070

improves the material's stability and longevity. Initially investigated as a cathode material in the context of LIBs as described by Barker et al.[28,29] NVPF attracted renewed fascination, serving as a cathode material for SIBs following its significant characterization by Shakoor et al.[30] This pioneering research established NVPF as a leading candidate for advanced SIB technologies, highlighting its potential for improved energy-storage solutions.

Nevertheless, their practical application remains constrained by inherent drawbacks such as low specific capacity, moderate electronic conductivity, sluggish sodium-ion transport, and capacity fading during extended cycling, thereby necessitating targeted structural and surface modifications.[31–34] To overcome these challenges, strategies such as carbon coating, nanoscale modification, and heteroatom doping have been explored.[35] Among them, ion doping notably enhances NVPF's electrochemical performance by improving structural stability and conductivity. Substituting V sites with ions like Mg^{2+}, Al^{3+}, Fe^{2+}, Mn^{2+}, Cr^{3+}, and Y^{3+} has led to significant improvements.[36]

Recent studies highlight notable electrochemical improvements in NVPF via doping and compositional optimization. Zhang et al. reported that 5 mol% Mg-doped NVPF@C delivered 126.8 mAh g^{-1} at 0.1C (where 1C = 128 mA g^{-1}) with 96.72% retention over 100 cycles.[37] In a related study, Zhuang et al.'s 7 mol% Al-doped sample achieved 103 mAh g^{-1} with a stable 99.9% Coulombic efficiency and retained 65 mAh g^{-1} after 400 cycles.[38] Yang et al. combined Fe doping with a 3D N-CNT/carbon framework, attaining 105 mAh g^{-1} at 0.1C and maintaining ≈74.5% capacity after 1000 cycles at 2C and 83.4% after 1200 cycles at 5C, demonstrating enhanced Na^+ transport and conductivity.[39] Su et al. reported that Mn^{2+} doped NVPF delivered a reversible capacity of 116.2 mAh g^{-1} at 0.2C and retained 67.7% capacity over 400 cycles at 1C, demonstrating improved capacity and cycling stability.[26] These results affirm that doping enhances the electrochemical performance of NVPF. However, despite initial gains, capacity retention often declines at high current densities, indicating that long-term stability remains a key challenge for doped SIB cathodes.

This study aimed to upgrade the high discharge capacity of NVPF by doping it with various Ti contents, synthesized via the sol–gel technique. We employ a targeted titanium doping concentration that facilitates a detailed understanding of how Ti content affects the electrochemical properties and structural stability of NVPF. The results reveal significant improvements in cycling stability and discharge capacity. Among the prepared samples, NVPF-Ti-0.02 demonstrated the best performance, achieving a specific discharge capacity of 133 mAh g^{-1} at a current rate of 50 mA g^{-1} and a capacity endurance of 94.76% over 100 cycles. These findings underscore the promise of Ti-doped NVPF as an efficient and stable cathode for advanced SIBs and large-scale energy storage.

2. Results and Discussion

$Na_3V_2(PO_4)_2F_3$, classified as a NASICON-type material, naturally supports the intercalation of sodium ions due to its relatively rapid ionic diffusion kinetics. However, its inherent electron conductivity is limited due to its semiconducting properties. To address this limitation, ion doping is a well-established technique for enhancing the intrinsic electron conductivity of such materials, as demonstrated by various studies.[36] In this study, titanium doping combined with carbon coating was employed to improve the electronic conductivity and overall efficiency of NVPF. The synthesis of titanium-doped, carbon-coated $Na_3V_{2-x}Ti_x(PO_4)_2F_3$@C samples was achieved using a sol–gel method, as detailed in the Experimental Section. These samples, denoted as NVPF-Ti-x, where x represents the molar fraction of Ti substituting the V atom (x = 0, 0.01, 0.02, 0.03, 0.04, and 0.05), allowing for uniform incorporation of titanium into the NVPF lattice, resulting in Ti-doped, carbon-coated variants. The values for x are determined by controlling the molar ratio of titanium (Ti) to vanadium (V) during the synthesis process. This is achieved by substituting a precise amount of Ti for V in the NVPF structure. In a typical sol–gel route, the molar amounts of Ti and V precursors are calculated to match the desired doping level. For example, when x = 0.01, 1% of the V atoms are replaced by Ti atoms, meaning the ratio of Ti to the total amount of V and Ti in the sample is 1:99. Similarly, when x = 0.02, 2% of V atoms are replaced by Ti atoms, and so on for the other values of *x*. The substitution level *x* is controlled by adjusting the relative amounts of the Ti and V precursors. A schematic illustration of the synthesis process is provided in **Scheme 1**, which delineates the various stages of the preparation. To verify the successful integration of Ti and the formation of the carbon coating, the structural characteristics of the synthesized particles were initially analyzed using X-ray diffraction (XRD). This analysis confirmed the incorporation of Ti into the lattice and the presence of the carbon coating, thereby validating the effectiveness of the doping and coating processes in enhancing the material's properties.

Figure 1a illustrates the XRD patterns of the as-synthesized NVPF-Ti-x (x = 0, 0.01, 0.02, 0.03, 0.04, and 0.05) gel precursors, which feature varying ratios of titanium oxide. The XRD patterns reveal distinct characteristic peaks corresponding to the (002), (220), (113), (222), (400), (331), (420), (315), and (440) planes. All diffraction peaks align with the tetragonal NVPF phase (JCPDS no: 01-089-8485) and align with a tetragonal symmetry within the P42/mnm space group. This alignment confirms that the incorporation of Ti does not modify the intrinsic crystal structure of NVPF. For these samples, no impurity peaks are detected, and the XRD peaks are sharp, indicating good crystallinity across all samples except for NVPF-Ti-0.05, which shows a slight reduction in crystallinity. In the corresponding Figure 1b with an enlarged XRD pattern, the peaks associated with the (220), (113), and (222) planes in NVPF-Ti-0.05 exhibit slight broadening and a shift toward higher 2-θ values with increasing Ti concentration, suggesting a slight contraction of the unit cell. This lattice shrinkage, caused by excessive Ti doping, reduces the sodium ion diffusion coefficient, leading to a decline in rate performance. This observation corroborates that the structural resilience of the authentic material is preserved when the Ti doping level is maintained below 0.05.

The ionic radius of Ti^{4+} (42 pm) is notably smaller than that of V^{3+} (64 pm), which confirms the successful incorporation of Ti into the NVPF crystal lattice in its tetravalent state.[40]

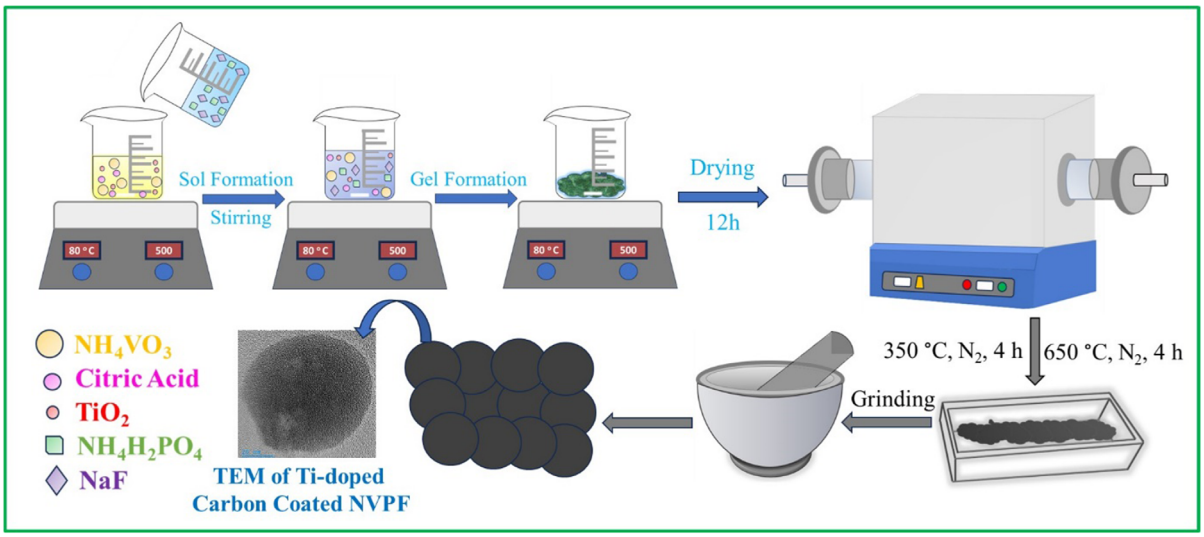

Scheme 1. Schematic depiction of the synthesis procedure for $Na_3V_{2-x}Ti_x(PO_4)F_3$@C samples.

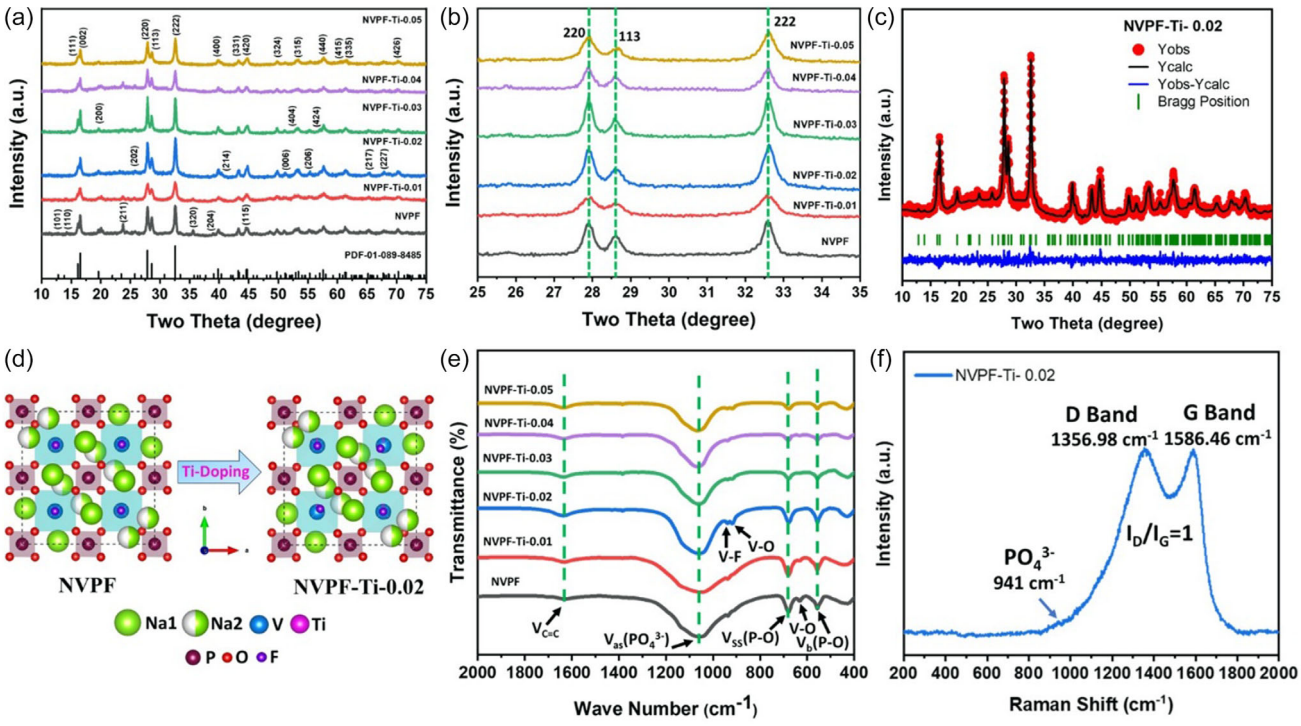

Figure 1. Structural characterizations of as-prepared NVPF-Ti-x (x = 0, 0.01, 0.02, 0.03, 0.04, and 0.05) samples: a) X-ray diffraction (XRD) pattern of different NVPF-Ti-x cathode materials with corresponding JCPDS card no. 01-089-8485, b) enlarged XRD patterns, c) Rietveld refined XRD pattern of NVPF-Ti-0.02 analyzed by FullProf Suite software, d) crystal structure of NVPF and NVPF-Ti-0.02, e) FTIR spectra of different NVPF-Ti-x cathode materials, and f) Raman spectrum of NVPF-Ti-0.02.

The substitution of V^{3+} with Ti^{4+} leads to shorter V—O and V—F bond lengths due to the reduced size of the Ti^{4+} ion. This substitution results in a contraction of unit cell volume, which in turn enhances the stability of the NVPF structure during electrochemical processes.[37] The shorter bond lengths provide more efficient transfer routes for Na^+ ions and electrons, consequently improving the intrinsic electronic conductivity of NVPF. The incorporation of Ti^{4+} into the NVPF lattice leads to the partial substitution of V, inducing slight differences in ionic radii and valence states between Ti^{4+} and V^{3+}/V^{4+}. The resulting shorter bond lengths/bandgap also help to reduce the Na^+ diffusion barrier, which facilitates more efficient pathways for Na^+ ion diffusion and electron transport, ultimately improving the intrinsic electronic conductivity of NVPF.[41] To gain a deeper understanding of the crystal structure of NVPF-Ti-0.02, Rietveld refinement was conducted (Figure 1c). The refinement revealed lattice

parameters of a = b = 9.042 Å, c = 10.713 Å, with $\alpha = 90°$, $\beta = 90°$, and $\gamma = 90°$, with a χ^2 value of ≈1.12. The refined cell volume was found to be 875.920 Å^3, which shows a slight reduction compared to the standard JCPDS data for NVPF, where a = b = 9.047 Å, c = 10.705 Å, and the cell volume is 876.185 Å^3 as well as less from as-synthesized NVPF refinement data as shown in Figure S1, Supporting Information, where a = b = 9.04189 Å, c = 10.72625 Å, and cell volume = 876.920 Å^3. This reduction in lattice parameters confirms the contraction of the lattice due to the substitution of V^{3+} with smaller Ti^{4+} ions in the Ti-doped NVPF. The XRD refinement results (Table S1 and S2, Supporting Information) clearly demonstrate that Ti^{4+} ions proficiently substitute for a portion of the V^{3+} sites within the crystal structure as depicted in Figure 1d. This finding affirms the effective inclusion of Ti^{4+} into the $Na_3V_2(PO_4)_2F_3$ framework. Additionally, the absence of carbon-related diffraction peaks suggests that the carbon is present as a disordered coating rather than in a crystalline form.

The Fourier transform infrared (FTIR) spectra of the synthesized NVPF samples are presented in Figure 1e, showcasing peaks in the range of 400–4000 cm^{-1}, indicative of well-defined crystallinity. Key peaks for all NVPF samples are noted as follows: the C═C bond stretching around ≈1630–1635 cm^{-1},[25] asymmetric stretching (V_{as}) of the PO_4^{3-} group, observed as strong broadband near ≈1050–1060 cm^{-1},[42] V—O bond vibrations identified by bands at ≈630 and 915 cm^{-1},[43] and V—F bond stretching at ≈935 cm^{-1}.[24] The introduction of Ti^{4+} in place of V^{3+} in the Ti-doped NVPF structure induces substantial changes within the lattice due to the smaller ionic radius of Ti^{4+}. This size difference results in shorter V—O and V—F bond lengths, causing a reduction in overall unit cell volume, which enhances the material's structural compactness. These modifications not only strengthen the crystal stability but also positively affect the electrochemical properties, promoting enhanced electron mobility and more efficient sodium ion diffusion during charge and discharge processes. Furthermore, bending vibrations (V_b) and symmetric stretching vibrations (V_{ss}) of the P—O bond were detected at ≈555 and ≈675–680 cm^{-1}, respectively.[37]

A comparative Raman spectroscopy analysis of pristine NVPF, NVPF-Ti-0.02, and NVPF-Ti-0.05, as shown in Figure S2, Supporting Information, elucidates the structural modifications induced by Ti doping at various concentrations. Additionally, Figure 1f provides a detailed Raman spectrum of the NVPF-Ti-0.02 sample. The spectrum depicted two dominant and broad peaks at a range of 1353–1360 cm^{-1} and 1586.46 cm^{-1}, corresponding to the D band and G band that represent disordered carbon and graphitic carbon, respectively.[44] The spectra in Figure S2, Supporting Information, reveal a distinct shift in the D band toward lower wavenumbers, from 1360 cm^{-1} in pristine NVPF to 1356.98 cm^{-1} in NVPF-Ti-0.02 and further to 1353.22 cm^{-1} in NVPF-Ti-0.05. The G band, however, remains consistent across all samples at 1586.46 cm^{-1}. The relative peak area ratio of the D and G bands, defined as the intensity ratio of the D band to the G band (ID/IG), serves as an indicator of the graphitization degree of the carbon coating.[45] In this study, pristine NVPF exhibits the lowest ID/IG value of 0.94, while the Ti-doped samples, NVPF-Ti-0.02 and NVPF-Ti-0.05, display progressively higher values of 1.00 and 1.03, respectively. This increase in ID/IG values for the Ti-incorporated samples signifies an enhancement in the graphitization of the residual carbon, likely facilitated by Ti doping. Improved graphitization in NVPF-Ti-0.02 and NVPF-Ti-0.05 is expected to contribute to increased electronic conductivity, thereby supporting the superior electrochemical performance observed in Ti-doped NVPF materials. Additionally, ID/IG = 1 indicates that nearly equal amounts of disordered and graphitized carbon are present in the synthesized material.[2] This balance between disordered and graphitic carbon suggests a well-developed carbon coating on the NVPF particles. In NVPF-Ti-0.05, the ID/IG ratio is larger than 1, suggesting a higher proportion of amorphous carbon within the material.[46] Moreover, the high intensities of both the D and G bands overshadow the peak at 941 cm^{-1}, which corresponds to the symmetric P—O stretching mode of the PO_4^{3-} group, suggesting a dominant carbonaceous influence in the NVPF samples.[2,47]

The scanning electron microscope (SEM) analysis of both undoped NVPF and Ti-doped NVPF, as depicted in Figure S3, Supporting Information, reveals significant morphological changes with varying levels of titanium doping. Both materials exhibit globular or oval shapes with inhomogeneous particle sizes and notable nanoparticle agglomeration. The undoped NVPF features particles ranging in size from 50 to 270 nm, characterized by significant agglomeration and inhomogeneous morphology due to high-temperature calcination. The introduction of titanium into NVPF results in notable changes in particle size. For the NVPF-Ti-0.01 sample, particle sizes range from 55 to 560 nm. As the Ti content increases, the particle sizes in the NVPF-Ti-0.02 sample expand significantly, ranging from 100 nm to 1.1 μm, with more pronounced agglomeration. This observation suggests that Ti doping initially leads to an increase in particle size, likely due to the modification of crystal growth mechanisms during synthesis.[48] For the NVPF-Ti-0.03 sample, particle sizes are observed within the range of 105 to 900 nm. With further Ti doping in the NVPF-Ti-0.04 sample, particle sizes extend from 110 nm to 1 μm, accompanied by increased agglomeration. Interestingly, in the NVPF-Ti-0.05 sample, the particle size distribution narrows to between 120 and 400 nm, indicating that excessive Ti doping leads to a reduction in particle size. **Figure 2**a–f shows SEM images of different magnifications (10–50 Kx) NVPF-Ti-0.02 sample. Among all the synthesized samples, the study suggests that NVPF-Ti-0.02 shows the largest particle size, followed by NVPF-Ti-0.04, while NVPF-Ti-0.05 among Ti-doped NVPF shows the smallest particle size. The ionic radius of titanium is smaller compared to that of vanadium. Furthermore, Ti incorporation influences the nucleation and growth dynamics by enhancing the nucleation rate while limiting particle growth. This effect stems from the reduced crystallization ability induced by Ti doping, which promotes heterogeneous nucleation, ultimately leading to the formation of smaller and more homogeneous particles.[48]

A similar trend has been observed in other ion-doped systems. This trend highlights the dual effect of Ti doping on NVPF morphology: initially increasing particle size, followed by a reduction as more Ti is incorporated. The observed increase and subsequent decrease in particle size with rising Ti content underscore the critical role of Ti doping in determining the final

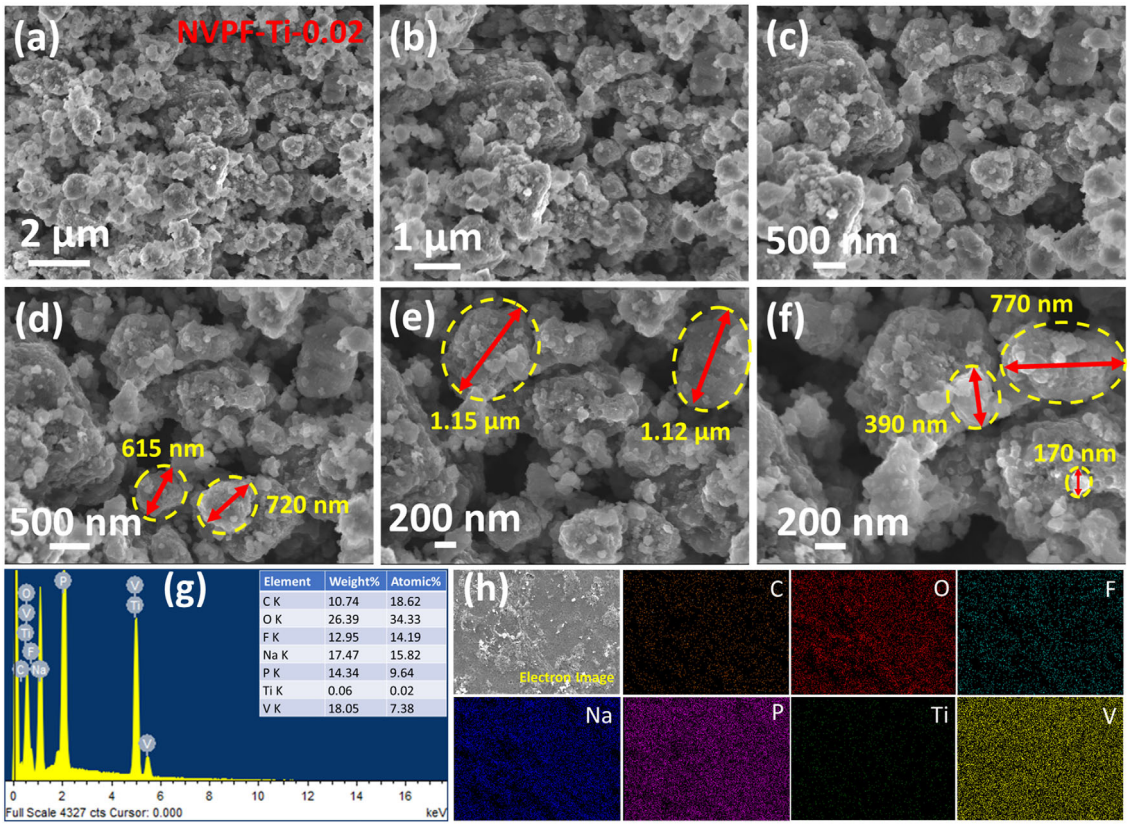

Figure 2. a–f) The SEM images of NVPF-Ti-0.02, g) the EDS energy spectrum of the NVPF-Ti-0.02 sample, and h) elemental color mapping of NVPF-Ti-0.02.

morphology and particle size distribution of NVPF-based materials, which could be key to optimizing their performance in SIBs.

Figure 2g illustrates the elemental distribution obtained from energy-dispersive X-ray spectroscopy (EDS) analysis, confirming the uniform distribution of C, O, F, Na, P, Ti, and V. The results indicate that oxygen is the most abundant element, comprising 26.39% by weight, which is consistent with the phosphate structure of NVPF. Sodium and vanadium follow, contributing 17.47% and 18.05% by weight, respectively, aligning with the expected stoichiometry of the NVPF composition. Phosphorus accounts for 14.34% by weight, indicating the presence of phosphate groups in the NVPF structure, and fluorine is about 12.95 % by weight. Carbon is present at 10.74% by weight, suggesting the presence of carbon coating. Titanium is detected at a low concentration of 0.06%, confirming the successful doping of Ti at minimal levels. The even distribution of carbon indicates that it not only coats the particle surfaces but also forms a conductive network, facilitating Na^+ and electron transport and thus improving the material's electrical conductivity. The presence of Ti and C further validates effective Ti doping and successful carbon encapsulation, which collectively enhance the structural and electrochemical properties of the NVPF material. Furthermore, in Figure 2h, elemental color mapping also confirms uniform distribution in NVPF-Ti-0.02, indicating that the composite sample was successfully synthesized.

The low-magnification transmission electron microscopy (TEM) images of the NVPF-Ti-0.02 sample, shown in **Figure 3**a and b, reveal that the majority of particles exhibit predominantly globular and oval-shaped morphologies, consistent with the SEM observations. These particles vary in size, ranging from ≈20 to 120 nm in length and 25 to 45 nm in width, and display significant agglomeration. High-resolution TEM (HRTEM) images of Figure 3c,d reveal distinct lattice fringes with lattice spacings of 0.23 and 0.28 nm, corresponding to the (204) and (222) crystal planes, respectively. Moreover, upon closer examination, the HRTEM image in Figure 3e distinctly highlights a lattice fringe with a d spacing of 0.28 nm, corresponding to the (222) crystal plane. Additionally, Figure 3d clearly shows a carbon layer present at the outermost layers of the particle. It provides a distinct view of the double-layered amorphous carbon coating, which has a thickness of ≈3.7 nm. The presence of this unique double-layered carbon matrix significantly enhances the surface electron conductivity of the NVPF-Ti-0.02 sample. Encasing NVPF particles in a thin layer of amorphous carbon serves a dual purpose: it effectively curtails particle growth, prevents excessive agglomeration, and simultaneously establishes a robust conductive pathway that significantly improves electron-transport efficiency.[49] This carbon coating also plays a crucial role in increasing the wetted surface area of the electrode, which is essential for optimizing the electrode–electrolyte interface. As a result, the kinetic properties during redox reactions are notably enhanced, leading to improved overall performance in electrochemical applications.

The selected area electron diffraction (SAED) pattern obtained from a particle of NVPF-Ti-0.02, as shown in Figure 3f, is consistent with the expected crystal planes. Specifically, the SAED corresponds to the (111), (002), (211), (113), (320), (204), (222), (420), (006), (424), and (335) planes. These results confirm the purity

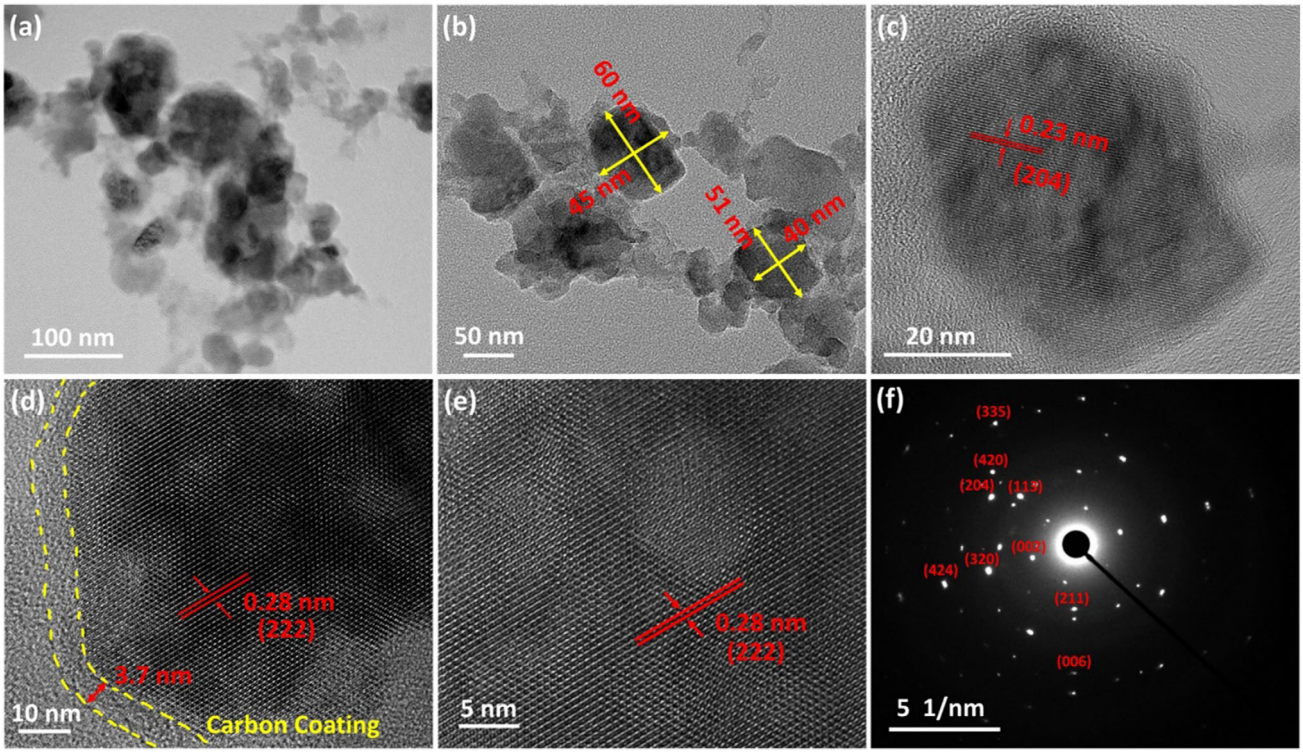

Figure 3. a,b) TEM images of NVPF-Ti-0.02, c–e) HRTEM images of particles illustrating lattice fringes and carbon coating, and f) SAED pattern of NVPF-Ti-0.02 particle.

and phase structure of the NVPF-Ti-0.02 material, as further corroborated by the XRD patterns presented in Figure 1a. Overall, the incorporation of a double-layered carbon coating and Ti doping in the NVPF structure enhances both the electron conductivity and rate capability, potentially leading to higher performance as a cathode material in SIBs. The improved electronic conductivity and ionic-transport properties due to these modifications contribute to the high performance of NVPF-Ti-0.02 as a cathode in SIBs.

X-ray photoelectron spectroscopy (XPS) is harnessed to interpret the chemical configuration and states of NVPF-Ti-0.02. In the XPS spectra, distinctive peaks for all seven elements, V, O, C, P, Ti, Na, and F, are detected, confirming the successful synthesis of Ti-doped NVPF material. These elements are attributed to V^{3+}, O^{2-}, P^{5+}, Ti^{4+}, Na^{+}, and F^{-}. The high-resolution V 2p spectrum of NVPF-Ti-0.02, shown in **Figure 4**a, reveals two distinct peaks at 522.63 and 515.5 eV, corresponding to V $2p_{1/2}$ and V $2p_{3/2}$, respectively. These peaks validate the existence of V^{3+} in the material.[39] Specifically, the peak at $\approx$ 515.5 eV is assigned to the V $2p_{3/2}$ orbital, which results from the spin–orbit interaction of vanadium in its oxidation state of +3. In the O 1s spectrum (Figure 4b), three peaks are observed at binding energies of 529.5, 530.7, and 533.8 eV. These peaks are attributed to the P—O bond, C—O bond, and the Na Auger electron transition involving K and L shells (KLL) Auger peak, respectively.[37] The presence of the C—O bond signifies that the carbon layer is not merely engrafted on the surface of the grains but is interacting with the underlying material. The C—O peak in the high-resolution O1s spectrum suggests strong bonding between the carbon coating and oxygen. Additionally, the Na KLL Auger peak further confirms the presence of Na^{+}. Peaks at binding energies of 283.1, 284.6, 286.7, and 288.9 eV are assigned to C—C, C—O, C═O, and O—C═O functional groups (Figure 4c), respectively, highlighting the successful carbon coating on the sample surface.[35] The single peak at 133.67 eV in the P 2p spectrum (Figure 4d) suggests a uniform chemical environment for phosphorus, most likely in the form of PO_4^{3-} groups.[38]

The subtle spectral features of Ti suggest a low Ti concentration in the sample (Figure 4e). The two distinct peaks associated with Ti $2p_{1/2}$ (460 eV) and Ti $2p_{3/2}$ (453.87 eV) confirm that the Ti present in the composite material is in the tetravalent state.[40] A singular peak for Na 1s (Figure 4f), located at 1069.87 eV, indicates the stable bonding and consistent oxidation state of sodium within the crystal lattice.[38] Additionally, the single peak observed at 682.63 eV in the high-resolution F 1s spectrum (Figure 4g) points to the presence of fluorine.[25] The complete XPS spectrum survey scan (Figure 4h) further reveals the presence of V, O, P, Na, and F as the primary elements, along with detectable amounts of C and Ti.[45]

To check the electrochemical performances of the as-prepared electrode, we performed different electrochemical tests, such as galvanic charge–discharge, cyclic voltammetry (CV), and electrochemical impedance spectroscopy (EIS) at 22 ± 2 °C against sodium foil in sodium fluorophosphate electrolyte medium containing ethylene carbonate/ propylene carbonate. The initial charge–discharge profiles of NVPF-Ti-x (x = 0, 0.01, 0.02, 0.03, 0.04, and 0.05) samples at 50 mA g^{-1} are presented in **Figure 5**a. The undoped NVPF sample delivered a primary discharge capacity of 101 mAh g^{-1}. Upon doping with Ti, a slight enhancement

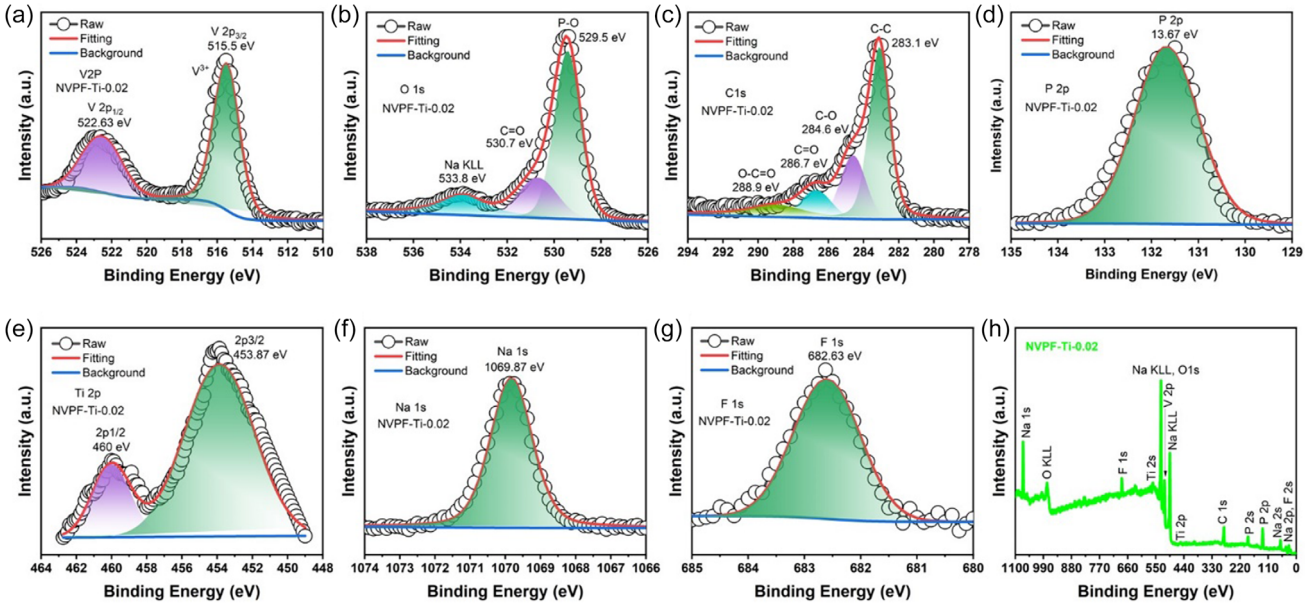

Figure 4. The XPS high-resolution spectra of the NVPF-Ti-0.02: a) V2p, b) O1s, c) C1s, d) P2p, e) Ti2p, f) Na1s, g) F1s, and h) survey scan of NVPF-Ti-0.02 confirming the presence of individual elements vanadium, oxygen, carbon, phosphorous, titanium, sodium, and fluorine.

in capacity was observed for NVPF-Ti-0.01, which achieved 105 mAh g^{-1}. Further increases in Ti content resulted in a significant improvement, with NVPF-Ti-0.02 exhibiting an initial first discharge capacity of 154 mAh g^{-1}. However, NVPF-Ti-0.02 achieved an exceptional stabilized specific capacity of 133 mAh g^{-1} at a current density of 50 mA g^{-1} from its second cycle onward. It showed a high reversible capacity retention of 94.76% after 100 cycles and 81% after 300 cycles. The initial capacity of the NVPF-Ti-0.02 sample exceeds the theoretical value (128 mAh g^{-1}), which corresponds to the extraction of two Na^+ ions per formula unit via the V^{3+}/V^{4+} redox couple. The partial substitution of V by Ti is believed to modify the local electronic structure and improve Na^+ diffusion kinetics, potentially activating additional redox processes such as the V^{4+}/V^{5+} couple or surface-related charge-storage mechanisms enabled by carbon coating and Ti doping.[50–52] These effects contribute to the elevated initial discharge capacity of 154 mAh g^{-1}. However, after the first cycle, Na^+ was trapped inside the NVPF-Ti-0.02 structure, and the V^{4+}/V^{5+} redox couple was no longer active, and this excess capacity is not fully sustained; the capacity stabilizes around 133 mAh g^{-1} from the second cycle onward and remains consistent over 50 cycles. This indicates that the long-term charge storage is primarily governed by the reversible V^{3+}/V^{4+} redox mechanism.[50–52] However, as the Ti content increased in NVPF-Ti-0.03, the initial discharge capacity decreased to 116 mAh g^{-1}. With additional increases in Ti content, NVPF-Ti-0.04 displayed a modest increase in initial capacity to 120 mAh g^{-1}, while NVPF-Ti-0.05 demonstrated a high initial discharge capacity of 144 mAh g^{-1}, though not as high as that of NVPF-Ti-0.02.

Figure 5b illustrates the cycling performance of the NVPF, NVPF-Ti-0.01, NVPF-Ti-0.02, NVPF-Ti-0.03, NVPF-Ti-0.04, and NVPF-Ti-0.05 at a current rate of 50 mA g^{-1}. The discharge capacities measured after 100 cycles were 96 mAh g^{-1} for NVPF, 101 mAh g^{-1} for NVPF-Ti-0.01, 126 mAh g^{-1} for NVPF-Ti-0.02, 108 mAh g^{-1} for NVPF-Ti-0.03, 114 mAh g^{-1} for NVPF-Ti-0.04, and 101 mAh g^{-1} for NVPF-Ti-0.05. The Coulombic efficiency of the undoped NVPF is 99.47%, which indicates high reversibility during cycling. In contrast, the Coulombic efficiency of the Ti-doped NVPF samples is lower: 99.24% for NVPF-Ti-0.01, 96.41% for NVPF-Ti-0.02, 98.94% for NVPF-Ti-0.03, 98.99% for NVPF-Ti-0.04, and 95.87% for NVPF-Ti-0.05 after 100 cycles. NVPF-Ti-0.02, which shows the highest discharge capacity of 133 mAh g^{-1} after the first cycle, exhibits the lowest Coulombic efficiency (96.41%). This suggests that, although Ti doping increases the capacity by enhancing Na^+ extraction, it also promotes side reactions, which consume some of the charge capacity and result in reduced reversibility during cycling. Among the Ti-doped samples, NVPF-Ti-0.02 achieved the highest discharge capacity. This is because the 0.02 level of Ti doping strikes an optimal balance between improving electronic conductivity and maintaining structural integrity. At this moderate doping level, the structural stability of NVPF is preserved. The ionic radius of Ti^{4+} is smaller than that of V^{3+}, so doping NVPF with Ti^{4+} results in the substitution of V^{3+} with Ti^{4+}. This substitution enhances electron transport and sodium-ion diffusion by reducing the V—O and V—F bond lengths and the unit cell volume, while also creating more robust channels for Na^+ intercalation and deintercalation in NVPF. The corresponding capacity retentions were 95.17%, 96.47%, 94.76%, 93.0%, 95.62%, and 76.10%. The discharge curve of NVPF-Ti0.05 does not exhibit two distinct voltage platforms, whereas the curves for lower titanium doping levels (0.01–0.04) do, primarily due to the suboptimal concentration of titanium in the 0.05 sample. At this doping level, the excess titanium may lead to unfavorable interactions within the structure, disrupting the phase transitions necessary for the formation of distinct sodiation and desodiation platforms.[51] Consequently, the balance between titanium concentration and structural integrity affects the electrochemical behavior of NVPF-Ti. This indicates that moderate Ti doping levels contribute positively to maintaining capacity over extended cycles, whereas higher doping levels, as

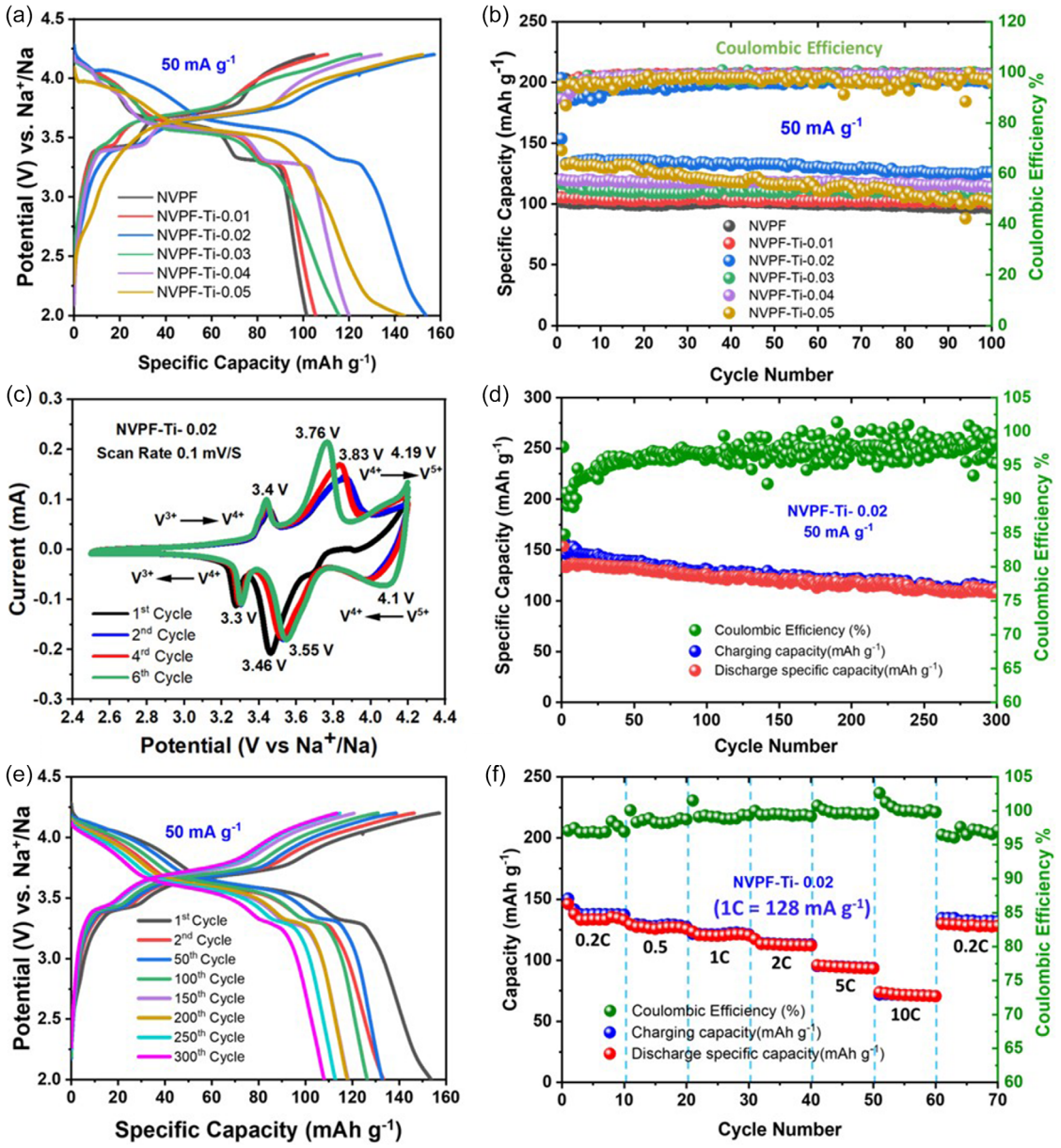

Figure 5. Electrochemical performance of Ti-doped NVPF in the voltage range of 2.0–4.2 V vs Na^+/Na: a) initial charge–discharge profiles at 50 mA g^{-1}, b) cycling performance at 50 mA g^{-1} of all NVPF and Ti-doped NVPF samples, c) cyclic voltammetry profile of NVPF-Ti-0.02 electrode from 2.5 to 4.2 V at 0.1 mV s^{-1}, d) long-term cycling performance of NVPF-Ti-0.02 at 50 mA g^{-1}, e) charge–discharge profiles of NVPF-Ti-0.02 at different cycles at 50 mA g^{-1}, and f) rate capability of NVPF-Ti-0.02 at various rates from 0.2C to 10C.

observed in NVPF-Ti-0.05, may reduce stability. At a Ti doping level of 0.05, the structural integrity begins to degrade, as indicated by XRD results. This leads to reduced stability and a decline in cycling performance, likely due to excessive distortion of the crystal lattice and compromised sodium-ion diffusion pathways. Notably, NVPF-Ti-0.02 and NVPF-Ti-0.04 exhibited superior long-term stability, with discharge capacities of 126 and 114 mAh g^{-1}, respectively, after 100 cycles, approaching the theoretical capacity of 128 mAh g^{-1}. While NVPF-Ti-0.05 initially demonstrated a high capacity of 144 mAh g^{-1}, its capacity began to fade with increasing cycles, eventually decreasing to 101 mAh g^{-1} after 100 cycles, resulting in the lowest capacity retention of 76.10%. These results suggest that optimal Ti doping can enhance the structural integrity and electrochemical performance of NVPF, while excessive doping may induce detrimental effects such as lattice distortion or phase transition,[51] as evidenced by the lower capacity retention of NVPF-Ti-0.05. Thus, the increase in rated capacity of 128 mAh g^{-1} for NVPF is attributed to titanium doping at the optimal level, which enhances structural integrity and improves both ionic and electronic conductivity.[52,53]

Figure 5c illustrates the CV behavior of the NVPF-Ti-0.02 electrode at a scan rate of 0.1 mV s^{-1}, within the potential window of 2.5–4.2 V (vs. Na/Na^+). The CV profiles exhibit three well-defined pairs of redox peaks, corresponding to the intercalation and deintercalation of Na^+ ions within the NVPF-Ti-0.02 structure, which are mainly governed by the V^{3+}/V^{4+} redox couple. The CV profiles

shown in Figure S4, Supporting Information, for pristine NVPF and Ti-doped NVPF-Ti-0.02 during the first and second cycles reveal distinct electrochemical characteristics that explain the capacity enhancement with Ti substitution. For the undoped NVPF, the redox peaks are primarily associated with the V^{3+}/V^{4+} redox couple. During the first cycle, oxidation peaks appear at ≈3.96 V, while in the second cycle, they are observed at 3.88 and 4.16 V. The corresponding reduction peaks are located around 3.44 and 3.71 V in the first cycle, shifting to 3.49 and 3.84 V in the second cycle. These peaks correspond to the reversible extraction and insertion of two sodium ions, which limits the theoretical capacity to ≈128 mAh g^{-1}. In contrast, NVPF-Ti-0.02 displays additional oxidation and reduction peaks at 3.4 and 3.3 V, respectively. Alongside these, high-potential oxidation and reduction peaks are observed near 3.85 and 3.46 V during the first cycle, with additional peaks at 4.19 V (oxidation) and 3.97 V (reduction) appearing in subsequent cycles. The presence of these extra peaks indicates activation of the V^{4+}/V^{5+} redox couple facilitated by Ti^{4+} substitution.[50] This enhanced redox activity directly correlates with the high initial discharge capacity of 154 mAh g^{-1} observed during the first cycle for the Ti-doped NVPF-Ti-0.02 sample. After an initial activation process during the first cycle, the capacity stabilizes around 133 mAh g^{-1} from the second cycle onward, closely matching the theoretical capacity. The first two pairs of peaks, occurring at lower voltages, are associated with the two-step Na^+ insertion and extraction at the Na2 sites in the NVPF lattice, while the third set of peaks around 4.19 V is linked to the insertion/extraction of the second Na^+ ion at the Na1 sites. During the anodic sweep, peaks observed at ≈3.4, 3.76, 3.83, and 4.19 V suggest a multistep oxidation process, with the 3.4 V peak indicating the onset of V^{3+} oxidation to V^{4+}, signaling the start of Na^+ removal. In the cathodic sweep, peaks at 4.1, 3.55, 3.46, and 3.3 V correspond to the reinsertion of Na^+ and the subsequent reduction of vanadium back to V^{3+}. The 4.1 V peak, occurring just after the 4.19 V oxidation peak, demonstrates the high reversibility of the redox process with minimal overpotential, indicating efficient Na^+ insertion and extraction. During the initial cycle, Ti doping introduces vacancies, leading to an activation process that gradually opens the active sites. As a result, some Na^+ ions become trapped within the structure and do not fully return to the cathode after the first cycle. This partial trapping reduces the total number of Na^+ ions participating in subsequent charge–discharge processes. Consequently, in the CV curves, the overall area under the discharge curve decreases after the first cycle, and the redox peaks shift to higher potentials, indicating increased polarization.[54]

During the first cycle, the peaks tend to be broader, and from the second cycle onward, the CV profiles become more uniform, showing consistent peak positions and shapes. By the fourth cycle, the CV curves demonstrate stable behavior, with the profiles for cycles 4 and 6 almost perfectly overlapping. This overlap indicates the structural endurance and excellent reversibility of the electrode material. The reduced polarization between anodic and cathodic peaks with repeated cycling reflects enhanced redox reversibility, likely due to the stabilization of the electroactive species and improved electrode interfaces. Additionally, the decreasing peak separation as cycling progresses suggests better efficiency in electron transfer and minimal material degradation and highlights the material's potential for long-term energy-storage applications. Additionally, Figure 5d shows that NVPF-Ti-0.02 maintained a discharge-specific capacity of 108 mAh g^{-1} after 300 cycles, with a capacity retention of 81% and a Coulombic efficiency of 95.33%. The low Coulombic efficiency of NVPF-Ti-0.02, around 95%, suggests significant side reactions between the electrolyte and the cathode material that led to capacity loss. Despite this, the enhanced structural stability of the material due to Ti doping suppresses irreversible phase transformations and improves ionic conductivity. As a result, we also observed low initial Coulombic efficiency during the charge–discharge process. These factors contribute to reduced charge transfer resistance, facilitating more efficient ion transport. As a result, even with the initial low efficiency, NVPF-Ti-0.02 demonstrates better capacity retention over cycles due to its enhanced structural integrity. The relatively high-capacity retention and stable Coulombic efficiency suggest that NVPF-Ti-0.02 exhibits excellent cycling stability and efficiency over extended use. This indicates that the Ti doping at this level effectively enhances the structural robustness and conduction of the NVPF material, allowing it to maintain good electrochemical performance and durability under prolonged cycling and varying current densities.

Figure 5e illustrates the charge and discharge capacities of NVPF-Ti-0.02 over various cycles. The material exhibited a discharge capacity of 154 mAh g^{-1} in the first cycle and 133 mAh g^{-1} in the second cycle. After 50 cycles, the discharge capacity was 133 mAh g^{-1}, which further decreased to 126 mAh g^{-1} over 100 cycles. At 150 cycles, the discharge capacity was 118 mAh g^{-1}, followed by 118 mAh g^{-1} over 200 cycles, 113 mAh g^{-1} over 250 cycles, and 108 mAh g^{-1} over 300 cycles. Notably, it retained a high capacity of 94.76% relative to the second cycle. NVPF-Ti-0.02 demonstrated superior rate performance, as evidenced by the different C rates (where 1C equates to a current density of 128 mA g^{-1}) presented in Figure 5f. The sample exhibited discharge-specific capacities of 133 mAh g^{-1} at 0.2C, 126 mAh g^{-1} at 0.5C, 120 mAh g^{-1} at 1C, 112 mAh g^{-1} at 2C, 93 mAh g^{-1} at 5C, and 70 mAh g^{-1} at 1C current density. When the current density is reverted to 0.2C after 60 cycles, the specific discharge capacity can be restored to 128 mAh g^{-1}, demonstrating a high recovery rate of ≈97%.

The EIS was carried out prior to electrochemical cycling to assess the effect of Ti doping on the charge transfer kinetics and interfacial resistance. As shown in **Figure 6**, the Nyquist plots of both undoped and Ti-doped NVPF samples reveal typical impedance features that can be divided into three regions: a small semicircle in the high-frequency region corresponding to the surface film resistance related to Na^+ ion migration across the electrode/electrolyte interface, a larger semicircle in the mid-frequency region attributed to the charge transfer resistance (R_{ct}), and an inclined line in the low-frequency region representing the Warburg impedance associated with solid-state diffusion of Na^+ ions within the electrode material.[3,55] The charge transfer resistance values obtained from the fitted data are 1430.76 Ω for undoped NVPF, 1152.00 Ω for NVPF-Ti-0.01, 584.40 Ω for NVPF-Ti-0.02, 727.90 Ω for NVPF-Ti-0.03, 1115.07 Ω for NVPF-Ti-0.04, and 1921.00 Ω for NVPF-Ti-0.05. Among these, the NVPF-Ti-0.02

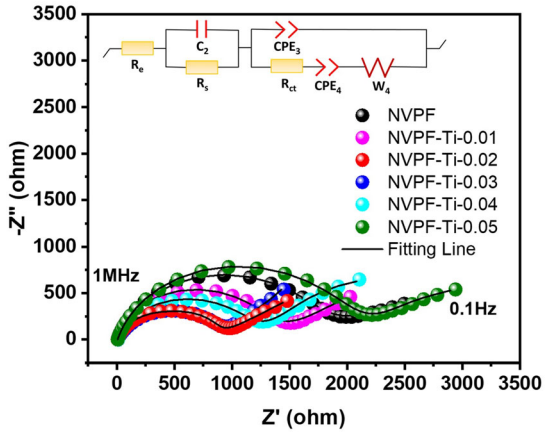

Figure 6. Nyquist plots of undoped NVPF and Ti-doped NVPF electrodes, illustrating overall electrochemical impedance.

sample exhibits the lowest R_{ct} value, indicating significantly enhanced charge transfer kinetics. This improvement is attributed to the synergistic effect of Ti substitution and uniform carbon coating, which together enhance ionic conductivity and reduce interfacial resistance. Additional EIS parameters, including surface film resistance, Warburg impedance, constant phase elements, and capacitance, are summarized in Table S3, Supporting Information. These observations collectively confirm that moderate Ti doping, particularly at the 0.02 mol level, is effective in optimizing the electrochemical performance of NVPF by facilitating faster sodium-ion insertion and extraction.

These results reflect the material's ability to deliver high discharge capacities across a range of current densities, indicating its robustness and good rate capability. Among the compared cathode materials, NVPF-Ti-0.02 (as demonstrated in Table S4, Supporting Information) exhibits significantly superior electrochemical performance. In contrast, NVPF@C/reduced graphene oxide reported by Al-Marri et al. (2025) achieved an initial first cycle discharge capacity of slightly lower capacity of 130 mAh g^{-1} at a current density of 0.5C,[56] while NVFNPF4, as reported by S. Mahato et al. (2025), delivers a much lower first-cycle capacity of 115.58 mAh g^{-1} at a lower current density of 0.1C.[32] The remarkable increase in reversible capacity of NVPF-Ti-0.02 during the first cycle can be attributed to a synergistic combination of structural, interfacial, and electrochemical modifications. A key mechanism involves the activation of the third sodium ion via the V^{4+}/V^{5+} redox couple, which increases the theoretical capacity of $Na_3V_2(PO_4)_2F_3$ from ≈128 to 192.3 mAh g^{-1}.[50,57] The incorporation of Ti^{4+} ions at the V sites is believed to stabilize higher oxidation states of vanadium during the charging process, thereby facilitating the activation of the V^{4+}/V^{5+} redox transition. This enables the extraction of a third Na^+ ion beyond the conventional two associated with the V^{3+}/V^{4+} redox couple, contributing to the high initial reversible capacity of 154 mAh g^{-1}. It delivers a high stabilized specific capacity of 133 mAh g^{-1} at 50 mA g^{-1}, maintaining this value consistently from the second cycle onward and remaining stable over 50 cycles. Moreover, it demonstrates excellent capacity retention of 94.76% after 100 cycles. Also, the uniform carbon coating enhances the interfacial contact between the active material and the conductive network, which creates additional surface-storage sites for Na^+ ions. A similar phenomenon was reported by Jeffry Nongkynrih in $Na_3V_{1.96}W_{0.04}(PO_4)_2F_3$@C, where extra capacity beyond the theoretical limit was attributed to beneficial interface effects between the active material and carbon matrix.[53] Jeffry Nongkynrih achieved a reversible capacity of 153 mAh g^{-1} at 0.1C using a W-doped NVPF@C material, attributing the enhanced capacity to interface-driven Na^+ storage and improved conductivity.[53] Similarly, Ketai Ren introduced 0.5 mol of Mg^{2+} in $Na_{3.5}V_{1.5}Mg_{0.5}(PO_4)_2F_3$ and attained a high capacity of 170 mAh g^{-1} within 1.0–4.7 V, enabled by the incorporation of additional Na^+ ions and activation of the V^{4+}/V^{5+} redox reaction.[57] These comparisons highlight the superior rate capability and outstanding cycling stability of NVPF-Ti-0.02, underscoring its potential as a highly promising cathode material for advanced SIBs. All the above results indicate that the titanium-doped NVPF will be a next-generation cathode material for SIBs for portable electronics applications.

3. Conclusions

The NVPF material was successfully synthesized, featuring a carbon-coated framework along with doping of titanium using a straightforward sol–gel method. Comprehensive investigations were conducted to assess the impact of Ti doping and carbon coating effects on the crystal framework, particle morphology, electrochemical behavior, and kinetic characteristics of NVPF. The incorporation of a disordered carbon layer was found to significantly enhance Na^+ transport by providing additional conduction pathways, thereby improving both surface electronic conduction and sodium-ion mobility kinetics. The presence of titanium in the structure was affirmed by XPS findings. Among the different doping levels tested, NVPF-Ti-0.02 exhibited the most favorable performance. It achieved a remarkable specific discharge capacity of 133 mAh g^{-1} at a current rate of 50 mA g^{-1} and demonstrated impressive capacity retention of 94.76% over 100 cycles. This cathode material also delivered an average energy density of 480 Wh kg^{-1}. Remarkably, NVPF-Ti-0.02 maintained a capacity value of 108 mAh g^{-1} over 300 cycles, equating to a capacity retention of 81%, with a stable Coulombic efficiency of 95.33%. The enhanced rate performance and superior cycling robustness of the titanium-doped composite address the common issues of low conductivity and capacity degradation observed in NVPF materials. These attributes underscore its potential as an excellent candidate for advanced SIBs and large-scale energy-storage applications.

Acknowledgements

The authors are indebted to the DRF Lab, Department of Chemical Engineering, IIT Kharagpur, for their assistance with FEG–SEM and FTIR spectroscopy. The authors also thank the Central Research Facility of IIT-KGP for providing access to XRD, XPS, and Raman spectroscopy testing facilities, as well as the SATHI Centre at IIT-KGP for the HRTEM analysis. Special thanks to all our colleagues for their continuous assistance and encouragement.

Conflict of Interest

The authors declare no conflict of interest.

Data Availability Statement

The data that support the findings of this study are available from the corresponding author upon reasonable request.

Keywords: cathodes · carbon coatings · $Na_3V_2(PO_4)_2F_3$ · sodium-ion batteries · Ti dopings

[1] P. Li, T. Yuan, J. Qiu, H. Che, Q. Ma, Y. Pang, Z. F. Ma, S. Zheng, *Mater. Sci. Eng. R Rep.* **2025**, *163*, 100902.
[2] W. Zhu, K. Liang, Y. Ren, *Ceram. Int.* **2021**, *47*, 17192.
[3] A. Sarkar, S. Sarkar, S. Mitra, *J. Mater. Chem. A* **2017**, *5*, 24929.
[4] A. Sarkar, A. K. Sinha, S. Mitra, *Electrochim. Acta* **2019**, *299*, 914.
[5] A. Sarkar, C. V. Manohar, S. Mitra, *Nano Energy* **2020**, *70*, 104520.
[6] A. Sarkar, S. Sarkar, T. Sarkar, P. Kumar, M. D. Bharadwaj, S. Mitra, *ACS Appl. Mater. Interfaces* **2015**, *7*, 17044.
[7] D. Wang, L. Teng, W. Liu, *Chem. Commun.* **2024**, *1*, 803.
[8] H. Watanabe, H. Usui, Y. Domi, T. Nishida, K. Uetake, T. Tanaka, H. Kurokawa, H. Sakaguchi, *ACS Electrochem.* **2025**, *1*, 73.
[9] J. A. K. Satrughna, A. R. Kanwade, S. M. Rajore, M. K. Tiwari, Y. Ito, A. Ogura, H. Lee, Y. Ohshita, P. M. Shirage, *Electrochim. Acta* **2024**, *507*, 145201.
[10] X. Chen, J. Chen, Z. Wan, Y. Hu, D. Duan, Y. Zhao, Q. He, *Small* **2024**, *2406458*, https://doi.org/10.1002/smll.202406458.
[11] A. Sarkar, S. Mitra, *J. Power Sources* **2020**, *452*, 227832.
[12] L. Han, S. Liao, S. Zhang, K. Chen, X. Chen, M. Li, Q. Li, X. Ai, Y. Cao, Y. Fang, *Sci. China Mater.* **2025**, *68*, 1109.
[13] R. Liu, S. Li, Z. Wang, H. Xu, W. Wang, Y. Jia, L. Zhang, Z. Xie, L. Wang, *Electrochim. Acta* **2025**, *522*, 145945.
[14] S. Guo, J. Peng, N. Sharma, J. Pan, Y. Liao, X. An, H. Li, Z. Ge, C. Zhou, W. L. Tan, J. Liu, *Chem. Mater.* **2025**, *2*, 1500.
[15] P. Naskar, S. Mondal, B. Biswas, S. Laha, A. Banerjee, *Sustain. Energy Fuels* **2023**, *7*, 4189.
[16] D. Zhou, C. Zeng, J. Xiang, T. Wang, Z. Gao, C. An, W. Huang, *Ionics Kiel* **2022**, *28*, 2029.
[17] J. Quan, E. Xu, H. Zhu, Y. Chang, Y. Zhu, P. Li, Z. Sun, D. Yu, Y. Jiang, *Phys. Chem. Chem. Phys.* **2021**, *23*, 2491.
[18] T. Chen, B. Ouyang, X. Fan, W. Zhou, W. Liu, K. Liu, *Carbon Energy* **2022**, *4*, 170.
[19] C. Shi, L. Wang, X. Chen, J. Li, S. Wang, J. Wang, H. Jin, *Nanoscale Horiz.* **2021**, *7*, 338.
[20] B. Xie, B. Sun, T. Gao, Y. Ma, G. Yin, P. Zuo, *Coord. Chem. Rev.* **2022**, *460*, 214478.
[21] A. Tyagi, S. Nagmani, *Sustain. Energy Fuels* **2022**, *6*, 550.
[22] Z. Lv, M. Ling, M. Yue, X. Li, M. Song, Q. Zheng, H. Zhang, *J. Energy Chem.* **2021**, *55*, 361.
[23] A. Zhao, Y. Fang, X. Ai, H. Yang, Y. Cao, *J. Energy Chem.* **2021**, *60*, 635.
[24] Y. Yang, G. R. Xu, A. P. Tang, J. C. Zheng, L. B. Tang, Y. De Huang, H. Z. Chen, *RSC Adv.* **2024**, *14*, 11862.
[25] Y. Qin, L. Li, H. Zhao, M. Wang, X. Li, J. Zhao, H. Wu, S. Ding, *CrystEngComm* **2022**, *24*, 4519.
[26] R. Su, W. Zhu, K. Liang, P. Wei, J. Li, W. Liu, Y. Ren, *Molecules* **2023**, *28*, 1409.
[27] M. Wang, Y. Wang, Y. Xin, Q. Liu, F. Wu, H. Gao, *ACS Appl. Energy Mater.* **2023**, *6*, 4453.
[28] R. K. B. Gover, A. Bryan, P. Burns, J. Barker, *Solid State Ionics* **2006**, *177*, 1495.
[29] J. Barker, R. K. B. Gover, P. Burns, A. J. Bryan, *Electrochem. Solid-State Lett.* **2006**, *9*, 190.
[30] R. A. Shakoor, D. H. Seo, H. Kim, Y. U. Park, J. Kim, S. W. Kim, H. Gwon, S. Lee, K. Kang, *J. Mater. Chem.* **2012**, *22*, 20535.
[31] W. G. Morais, E. C. Melo, R. M. Torresi, *Mater. Adv.* **2024**, *5*, 5070.
[32] S. Mahato, K. Biswas, *J. Power Sources* **2025**, *626*, 235734.
[33] Q. Fu, F. Song, C. Mu, Q. Wu, K. Wang, S. Li, X. Ao, *Energy Storage Mater.* **2025**, *74*, 103960.
[34] X. Yang, M. Wang, X. Xiang, S. Liu, C. Chen, *J. Electroanal. Chem.* **2024**, *956*, 118088.
[35] J. Zhang, C. Zhang, Y. Han, X. Zhao, W. Liu, Y. Ding, *RSC Adv.* **2024**, *14*, 13703.
[36] Y. H. Chen, Y. H. Zhao, S. H. Tian, P. F. Wang, F. Qiu, T. F. Yi, *Compos. Part B Eng.* **2023**, *266*, 111030.
[37] Y. Zhang, Y. Hu, T. Feng, Z. Xu, M. Wu, *J. Power Sources* **2024**, *602*, 234337.
[38] S. H. Zhuang, C. C. Yang, M. Zheng, S. Rengapillai, S. Marimuthu, Y. S. Chiang, B. K. Chang, C. H. Huang, W. R. Liu, *Surf. Coatings Technol.* **2022**, *434*, 128184.
[39] J. Yang, N. Liu, G. Jiang, W. Sheng, X. Zheng, Z. Bai, X. Jiang, *Chem. Eng. J.* **2024**, *485*, 149834.
[40] H. Yi, M. Ling, W. Xu, X. Li, Q. Zheng, H. Zhang, *Nano Energy* **2018**, *47*, 340.
[41] Q. Hu, M. Sun, Y. Zha, G. Zhao, H. Tang, L. Yang, M. Yang, B. Pang, Y. Sun, H. Guo, *ACS Energy Lett.* **2025**, *2*, 1840.
[42] S. Xu, H. Li, X. Wang, *ChemElectroChem* **2021**, *8*, 866.
[43] Z. Y. Gu, J. Z. Guo, Z. H. Sun, X. X. Zhao, W. H. Li, X. Yang, H. J. Liang, C. De Zhao, X. L. Wu, *Sci. Bull.* **2020**, *65*, 702.
[44] P. R. Kumar, Y. H. Jung, D. K. Kim, *J. Solid State Electrochem.* **2017**, *21*, 223.
[45] D. Ma, L. L. Zhang, T. Li, C. Liu, G. Liang, Y. X. Zhou, X. L. Yang, *Electrochim. Acta* **2018**, *283*, 1441.
[46] Q. Liu, D. Wang, X. Yang, N. Chen, C. Wang, X. Bie, Y. Wei, G. Chen, F. Du, *J. Mater. Chem. A* **2015**, *3*, 21478.
[47] J. He, T. Tao, F. Yang, Z. Sun, *ChemSusChem* **2022**, *15*, e202102522.
[48] Y. Wu, L. Fan, Q. Liu, S. Chen, W. Huang, F. Chen, G. Liao, C. Zou, Z. Wu, *Sci. Rep.* **2015**, *5*, 9328.
[49] C. Sun, L. L. Zhang, Z. R. Deng, H. Bin Sun, X. L. Yang, *ACS Appl. Mater. Interfaces* **2024**, *16*, 35179.
[50] M. Zhou, X. Zhou, L. Li, X. Chen, Z. Qiao, S. Chou, *Chem. Sci.* **2024**, *15*, 8651.
[51] S. Tong, H. Pan, H. Liu, X. Zhang, X. Liu, M. Jia, Y. Kang, Y. Yuan, X. Du, X. Yan, *ChemSusChem* **2023**, *16*, e202300244.
[52] C. Sun, L. L. Zhang, X. Q. Xiong, Z. R. Deng, H. Bin Sun, X. L. Yang, *ACS Sustain. Chem. Eng.* **2024**, *12*, 10892.
[53] J. Nongkynrih, A. Sengupta, B. Modak, S. Mitra, A. K. Tyagi, D. P. Dutta, *Electrochim. Acta* **2022**, *415*, 140256.
[54] K. Tang, H. Tian, Y. Zhang, Y. Cai, H. Ren, Y. Wang, X. Yao, Z. Su, *Energy Fuels* **2024**, *38*, 18035.
[55] J. Zhang, Y. Y. Lai, P. Li, Y. Wang, F. Zhong, X. Feng, W. Chen, J. Liu, X. Ai, H. Yang, Y. Cao, *Green Energy Environ.* **2022**, *7*, 1253.
[56] A. H. Al-Marri, *Ionics Kiel* **2024**, *31*, 427.
[57] K. Ren, J. Qiu, H. Liu, H. Song, Q. Li, J. Li, *ACS Appl. Energy Mater.* **2025**, *8*, 3066.

Manuscript received: February 10, 2025
Revised manuscript received: May 16, 2025
Version of record online: